EFDA–JET–PR(11)46

M. Rack, A. Wingen, Y. Liang, K.H. Spatschek, D.M. Harting, S. Devaux
and JET EFDA contributors

Thermoelectric Currents and their Role during ELM Formation in JET

Thermoelectric Currents and their Role during ELM Formation in JET

M. Rack[1,2], A. Wingen[1], Y. Liang[2], K.H. Spatschek[1], D.M. Harting[2], S. Devaux[3] and JET EFDA contributors*

JET-EFDA, Culham Science Centre, OX14 3DB, Abingdon, UK

[1]Institute of Theoretical Physics I, University of Düsseldorf, D-40225 Düsseldorf, Germany
[2]Institute of Energy and Climate Research/Plasma Physics, Forschungszentrum Jülich GmbH, Association EURATOM-FZJ, Partner in the Trilateral Euregio Cluster, D-52425 Jülich, Germany
[3]Max-Planck-Institut für Plasmaphysik, EURATOM-Association, D-85748 Garching, Germany
[9]Association EURATOM-VR, Department of Physics, SCI, KTH, SE-10691 Stockholm, Sweden
** See annex of F. Romanelli et al, "Overview of JET Results", (23rd IAEA Fusion Energy Conference, Daejon, Republic of Korea (2010)).*

Preprint of Paper to be submitted for publication in
Nuclear Fusion

ABSTRACT.
A recently developed numerical model, describing a self amplification and structure formation process which is used to model the initial non-linear growth phase of Edge Localized Modes (ELMs), is applied to the JET tokamak. Connection length simulations of the magnetic topology, including only error fields, for JET reveal the existence of small, so called short connection length flux tubes. Such a configuration is used as starting point for the model. Thermoelectric currents are assumed to flow in the short connection length flux tubes and add additional magnetic perturbations which change the magnetic topology severely. The change in magnetic topology leads to the formation of new, much larger short connection length flux tubes that can conduct much larger currents through the plasma edge. The current density inside the flux tubes is assumed to be constant to calculate the total current. This self amplification process leads to the formation of patterns, known as footprints, on various segments of the inner wall throughout the vessel. The resulting footprints and their relation to observed ELM patterns during discharges are discussed.

1. INTRODUCTION

Edge Localized Modes (ELMs) are of major interest to fusion science since the first ELMs were observed during H-mode operations of the ASDEX tokamak in the 1980s [1]. An ELM leads to fast, repeating losses of energy and particles from the plasma edge, resulting in peaked heat fluxes onto the plasma facing components. Calculations for ASDEX Upgrade result in heat fluxes as high as 20MW/m^2 [2] and about 80MW/m^2 for JET [3]. Such energy fluxes are known from the re-entry of space shuttles. For the planned fusion reactor ITER the expected heat flux due to ELMs is much higher due to the larger dimension of the device when compared to JET. This may cause major damage to the plasma vessel, like surface cracking and melting [4]. Existing theories describe ELMs as a mixture of pressure-driven and current-driven instabilities, the peeling-ballooning instability [5]. An ELM occurs when the edge pressure gradient becomes too steep; it continues until the pressure is reduced to a sufficiently low value. Experiments on DIII-D, JET and ASDEX Upgrade have shown that additional Resonant Magnetic Perturbation (RMP) coils can mitigate or suppress large ELM energy losses [6, 7, 8, 9, 10]. The RMP fields ergodise the magnetic plasma edge. It is believed that the edge ergodisation leads to reduction of the edge pressure gradient to stabilise the ELM, but the process is not yet understood in detail, especially the plasma response to the RMP fields that may modify the applied fields substantially. The physics of ELMs is still poorly understood and needs much more investigations. This paper will focus on the initial non-linear growth phase of the ELM instability.

A promising approach to improve the understanding of ELMs is the concept of additional currents in the Scrape-Off Layer (SOL) and/or plasma edge region that occur directly linked to ELMs. It is not aim of this work to give a self-consistent model as in references [11, 12]. This work focus on the magnetic topology influenced by the additional currents. Observations at many divertor experiments show a thermal difference between the inner and the outer targets during H-mode discharges. This

thermal difference can drive thermoelectric currents [13, 14]. In 1989 measurements of current flows in the JET SOL were mentioned by Harbour et al. [15]. These current flows appeared to be strongly linked to the observed ELMs. The measured current flow densities are stated as up to 7A/cm^2 at the targets. Harbour et al. detected that the current flows from the outer target through the SOL to the inner target. Such currents produce an additional magnetic perturbation resulting in severe changes of the magnetic topology, especially for large currents [16, 17]. This has a strong influence on the ergodisation of the plasma edge and may have a major role in the appearance of ELMs. Such currents are also observed during L-mode discharges, but compared to H-mode discharges are much smaller [14] and therefore could be neglected for L-mode calculations.

The numerical method is based on an extension of the vacuum field approach. Short connection length flux tubes [18] caused by the intrinsic error field are assumed to conduct additional currents. These currents are assumed to be thermoelectric currents. The influence of these currents on the magnetic topology, especially on the footprint structure, is investigated numerically in this paper. $\vec{j} \times \vec{B}$ forces, possibly leading to interactive, i.e. non-linear forces between such current carrying flux tubes, cannot be described self-consistently in this generic ad-hoc model. However, such forces would not lead necessarily to a major change of the actual divertor footprint area. Forces between the current carrying flux tubes will be dominant in the pedestal region where the distance is much shorter than at the divertor target due to the poloidal flux expansion. Calculations based on this model for DIII-D [19] result in the numerical reproduction of experimentally observed ELM stripe structures on the divertor targets, as observed e.g. for DIII-D, ASDEX Upgrade [20] and non-axis remnant of the ELM crash [21].

In the presented paper we validate the model, first published in reference [19], by calculations for JET. The comparison of predicted penetration depth profiles of field lines with measured heat flux profiles during an ELM crash shows good agreement. Section 2 describes the creation of short connection length flux tubes and discusses their special properties in contrast to stochastic regions. The implementation of the thermoelectric currents and their influence on the magnetic topology is investigated in section 3. In section 4 the predictions by the model are compared to experimental measurements of a fast infra-red camera [3] resulting in good agreement. The paper ends with a short summary and conclusion.

2. FLUX TUBE FORMATION

The vacuum model considers only magnetic fields, generated by external currents and the plasma equilibrium current, but neglects any further plasma effects. By using an Hamiltonian representation of the magnetic field, we can trace the field lines by solving the equations of motion

$$\frac{dR}{d\varphi} = R\,\frac{dR}{d\varphi} \quad , \tag{1}$$

$$\frac{dZ}{d\varphi} = R\,\frac{B_Z}{B} \quad . \tag{2}$$

(R, φ, Z) are cylindrical coordinates, with the major radius R and the toroidal angle φ. The total magnetic field $\vec{B}$ (R, φ, Z) = (B_R, B_φ, B_Z) includes an equilibrium reconstruction (EFIT) of an actual discharge as well as the RMP field of the external coil system. The latter is modelled by a Biot-Savart integrator [22].

In the following we extend the vacuum model to include additional plasma currents. These currents are motivated by the observed thermoelectric current between the outer and the inner targets. The presented calculations are based on the H-mode JET discharge JET Pulse No: 79459 at 15.918s (magnetic field of B_t = 2.7T, plasma current of I_P = 2MA and additional heating power of 9.7MW). In figure 1 a connection length calculation of the poloidal cross-section of the X-point region at the lower divertor is shown. The vacuum field of the JET discharge with a modelled intrinsic error field (I_{EFCC} = 1.6kAt at a n = 1 configuration) is calculated. At JET the intrinsic error field is not know, as a mockup the external field applied by the error field correction coils (EFCC) is used to model this intrinsic error field. The approximately squared EFCC are mounted out of the vacuum vessel, have a dimension of 6m and are arranged with four-fold symmetry. The broken and solid lines in figure 1 show the stable and unstable separatrix manifolds [23]. By the intersection of one inward loop of the stable and one inward loop of the unstable separatrix manifolds, we observe the creation of a so called short connection length flux tube [18], corresponding to the blue region in the figure. This flux tube is unaffected by the stochastic fractal nature of the perturbed edge region, because it is outside of the stable and unstable manifold plasma boundary. It connects the outer and inner target within only two poloidal turns, but is still embedded in the stochastic plasma edge surrounded by much longer field lines. Field lines from the stochastic plasma edge cannot enter the flux tube, but particles from this region can diffuse into the short connection length flux tube. Particles in the flux tube are lost to the targets on the time scale of parallel ion convection, typically observed in a range of a few 100μs [3]. In the presented model such flux tubes are assumed to conduct the thermoelectric current from the outer to the inner target.

Figure 2 shows the same poloidal cross-section as figure 1, but the crosses mark the points of penetration of a selected field line passing through flux tube 1. As we can see from the figure, all observable short connection length regions belong to the same flux tube, because they are connected by the same field line. Due to the fact that flux tubes are area preserving, these regions are identical in size. Such flux tubes are inside the separatrix and not in the SOL, have roughly twice the connection length of SOL currents. We assume that the currents in the additional flux tubes also have a same current as carried by the thermoelectric effect. The short connection length flux tubes are set in the outermost plasma edge, thus very close to the unperturbed SOL.

In DIII-D the amount of current running through the flux tubes was related to current measurements on the outer target [24]. Unfortunately such measurements do not exist for JET any more. Therefore, we assume a current density of 6A/cm^2 at the outer target which leads to the same current in the first flux tube as in the model for DIII-D. This assumption corresponds to the measured current density of the SOL currents in Ref. [15].

Figure 3 presents the connection length plot of the footprint on the outer target created at the strike-point of the finger-like stripe in figure 1. A footprint is given by the starting point of all field lines on one target that connecting this target to the other and fulfill more than one poloidal turn. From the footprint we observe the position of the touch-point of the observed short connection length flux tube, labelled as "flux tube 1". We can see another short connection length flux tube in the apex of the stripe, as well. It is much smaller in size so it could not be observed in the figure showing the poloidal cross-section. Because of its minor size, we neglect any current flow through this flux tube. To calculate the current, flowing through flux tube 1, we measure the contact area of this flux tube with the target. This area can be determined to 38.9 cm^2 from the calculated footprint in figure 3. With the assumed current density of 6A/cm^2, we assume a total current of 233A for flux tube 1. Because of the later requirement, we can also calculate the corresponding current density in the poloidal cross-section. The same flux tube has an area, about one magnitude smaller, in the poloidal cross-section, resulting in a current density of 202A/cm^2 in the poloidal cross-section.

3. THERMOELECTRIC CURRENTS

The current in the flux tubes is numerically implemented by line currents (here called filaments). There are two different ways to do this. Either the current is represented by one or two line currents with a large amount of current, or the total current is split into many filaments where each filament carries only a small fraction of the current. The latter approximates a uniform current density throughout the flux tube, while the former assumes a self-contraction of the currents. Both methods are reasonable and it is not yet decided if one method is more accurate then the other. The numerical simplest approach which we used here is the self-contraction of the current in the flux tubes.

Figure 4 shows a connection length plot in the poloidal cross-section in the vicinity of the lower divertor, perturbed by the field of the intrinsic error and one additional current filament in flux tube 1. We can observe the increase of the level of the stochasticity visible by the creation of many new short connection length flux tubes. Some of the new flux tubes are located at much smaller values of minor radius a than flux tube 1. Additionally we observe that most of the new flux tubes are larger in cross-section. The number of strike-points on the inner and outer target increases. In figure 5 a connection length plot of the footprint on the outer target is presented.

Compared to figure 3 the footprint has grown considerably on the target area because of the additional perturbation [25]. The outer, as well as the inner, structure of the footprint stripes have changed. The increase of the perturbation field has also an influence on the penetration depth of the field lines starting from the outer target. We calculated a total minimal normalised flux of about $\psi_{Min} = 0.796$. For the case of the vacuum approximation, i.e. without any currents in the flux tubes, a total minimal normalised flux of only $\psi_{Min} = 0.992$ is found.

Figure 6 is a magnification of figure 4 close to the X-point. Due to the additional magnetic perturbation of the current filament in flux tube 1 we observe eight new flux tubes. The cross-sections of the diverse flux tubes are numbered for later identification. Unlabelled short connection length

regions belong to the same flux tubes as the already denoted ones. All the flux tubes connect the inner and the outer target within two poloidal turns. From the measurement of the size of the flux tube cross-section we calculate the assumed currents flowing through these flux tubes (see table in figure 7). Some of the flux tubes carry a current of up to 1.1kA. In total the flux tubes carry an additional current of about 4.2kA. This results in a strong magnetic perturbation, changing the magnetic topology considerably (see figure 8).

The connection length plot of the poloidal cross-section in figure 8 is calculated at the same toroidal angle at which the infra-red camera observes the target. In comparison to figure 4 we notice a large displacement of the X-point and a strong increase of the stochasticity in the plasma edge region. Due to the strong total current in the flux tubes the X-point is shifted 4.3 cm downwards. The reason for this is that each current filament passes the X-point three times on its way from the outer to the inner target. Starting on the outer target the filament passes the X-point at the outer side, during the inner turn it passes the X-point from above and shortly before the filament hits the inner target it passes the X-point at the inner side. On average the magnetic fields resulting from the outer and inner pass roughly annihilate each other at the X-point, but the inner turn above the X-point leads to a total poloidal magnetic field at the old X-point position. Given, that the X-point is the position with vanishing poloidal field, it shifts, depending on the current strength and direction. This results in an inward shift of the magnetic strike-point on the inner and the outer targets toward lower Z, respectively R-vales. In figure 8 we observe a large increase of the number and larger area in poloidal cross-section of the finger-like structures. The whole inner target is connected to the plasma by the finger-like structures. Also the half of tile #5 is touched by very long fingers. Other connections to the wall do not exist. The strong connection of the plasma to the inner and outer targets results in a large particle and heat flux to the target plates. In contrast to the connection length plot in figure 4 the fingers have a stochastic structure due to the large number of asymmetrical perturbation fields. We can also see a much larger perturbation of the edge plasma region. This comes along with a large increase of the penetration depth of field lines starting on the outer target.

4. COMPARISON TO EXPERIMENTAL MEASUREMENTS

Depending on the penetration depth of the magnetic field lines particles with different energies will be carried towards the plasma wall along these field lines. Field lines with a large penetration depth connects the hot plasma region to the plasma wall and therefore high energetic particles are transported along these field lines to the wall. In contrast field lines with a low penetration depth stay close to the plasma edge region and only carry particles with a lower energy. A large increase of the number of field lines that penetrates deep into the plasma affects a similar increase of the number of high energetic particles that can be carried out from the hot plasma region along the field lines toward the plasma wall. This will result in strong heat flux to the target at that regions where higher penetration depth is predicted (see MASTOC criterion [26]). This heat flux is measured in JET by a fast infra-red camera (KL9). In figure 9 and figure 10 the heat flux and penetration depth

profiles for the same toroidal angle during the growth phase of the ELM are given. The heat flux profile is calculated from the KL9 data at the time t = 15.9214s. To calculate the penetration depth profile the average of the determined ψ_{Min} at the toroidal angles of the infra-red camera is taken. Ignoring the peaked nature of the calculated penetration depth profile we find good agreement with the measured heat flux profile in figure 9. Separated by the local minimum at Z = −1.56m the calculation shows two regions of large penetration depth. A lower one on the right hand side of the minimum and a stronger one on the left hand side. Two maximums separated by a local minimum are measured by the infra-red camera, as well. The position of the minimum is localised at the predicted position. The heat flux is strongly reduced at Z = −1.61m. From the prediction we can observe non-vanishing penetration depth at this position. The penetration depth drops at Z = −1.615m, shifted by 0.5cm. This is within the experimental error bars, i.e. misalignment of the infra-red camera and inaccuracy of the magnetic reconstruction. Not predicted by our model is the magnitude of the heat flux, but from the comparison of the heat flux at tile #3 we observe that the relative strength of the heat flux between both maximums may be predictable. The absolute maximum in the heat flux measurement appears at the same position as the maximum in the penetration depth profile.

Figure 10 shows the comparison of the measured heat flux profile and the penetration depth profile on the outer target, tile #5. The main maximum in the measured heat flux profile consists of four to five overlapping peaks. At the same position our model predicts four separated peaks of large penetration depth. All predicted peaks have nearly the same size. The local minimum between the two regions of larger heat flux appears in both profiles at the position R = 2.765m. On the right hand side of this minimum we observe four overlapping heat flux peaks. Peaks at these positions are also observed in the penetration depth profile. The large peak of penetration depth at R = 2.795m corresponds to a medium peak in the heat flux profile. The positions of the other heat flux peaks agree well with the prediction. The size of the peaks does not always correspond to the size of the measured heat flux. Nevertheless the relative amount of heat flux between both heat flux regions is predicted in this comparison. For the region with the large heat flux of up to 48MW/m^2 the calculation predicts larger penetration depth than for the second heat flux region.

DISCUSSION AND CONCLUSION

The presented model demonstrates the important role of magnetic perturbations by current filaments in the plasma edge during ELMs. It is an extension of the vacuum model. The vacuum model itself contains only the equilibrium reconstruction of an actual plasma discharge and the RMP field of an external coil system. No plasma effects, e.g. plasma response on the external perturbation fields, are included. In this paper we discuss the extension of the vacuum model, now taking certain plasma responses into account. A method to consider the currents in the plasma edge is presented. The numerical simplest approach of self-contraction currents leads to the successful agreement of the predicted penetration depth profiles and measurements. Since the presented model is a static model, $\vec{j} \times \vec{B}$ forces between the current filaments are not taken into account. The currents are motivated

by experimentally observed thermoelectric currents in the SOL that seem to be directly linked to ELMs. Even though the amount of current running through the flux tubes is not directly related to measurements from the experiment, the predictions fit to experimental observations of heat flux patterns at target tiles during JET discharges. The detailed comparison of the measured heat flux profiles and the predicted penetration depth profiles showing a wide range of qualitative agreements. The penetration depth, obtained from our model, cannot predict the amount of heat flux measured in the experiment. Nevertheless it seems to be possible to deduce the position of the heat flux pattern on the target from the penetration depth calculations. Small differences in the predicted and measured profiles are detected. These might be due to misalignment of the infra-red camera and inaccuracy of the magnetic reconstruction.

As this work focus on the changes of the magnetic topology due to the additional magnetic perturbations, particle effects itselfs are not investigated. Based on the presented results a more advanced analysis by a plasma edge transport model, e.g. provided by the EMC3-EIRENE code [27, 28], will be necessary to predict the amount of heat and particle flux at the target tiles.

The influence of additional currents connecting the targets seems to be a fruitful approach to model ELMs. ELM physics is an ongoing topic for fusion scientists. The calculations of this model result in good reproductions of experimental observations. Anyhow the process of ELM crash and the involved time-scales are not yet fully understood.

ACKNOWLEDGMENTS

Valuable discussions on the experimental observations of current filaments with Thomas Eich are gratefully acknowledged. This work, supported by the European Communities under the contract of Association between EURATOM and FZJ, was carried out within the framework of the European Fusion Development Agreement. The views and opinions expressed herein do not necessarily reflect those of the European Commission. Additional support from the Helmholtz Association in frame of the Helmholtz-University Young Investigators Group VH-NG-410 is gratefully acknowledged.

REFERENCES

[1]. ASDEX Team 1989 Nuclear Fusion **29** 1959

[2]. Zohm H 1996 Plasma Physics and Controlled Fusion **38** 1213

[3]. Eich T, Thomsen H, Fundamenski W, Arnoux G, Brezinsek S, Devaux S, Herrmann A, Jachmich S, Rapp J and JET-EFDA contributors 2011 Journal of Nuclear Materials doi:10.1016/j.jnucmat.2010.11.079

[4]. Linke J, Akiba M, Bolt H, Breitbach G, Duwe R, Makhankov A, Ovchinnikov I, Rödig M, Wallura E 1997 Journal of Nuclear Materials **241-243** 1210

[5]. Wilson H.R, Cowley S C, Kirk A and Snyder P B 2006 Plasma Physics and Controlled Fusion **48** A71

[6]. Evans T.E, et al 2004 Physical Review Letters **92** 235003

[7]. Liang Y et al 2007 Physical Review Letters **98** 265004
[8]. Liang Y et al 2010 Nuclear Fusion **50** 025013
[9]. Jachmich S, Liang Y, Arnoux G, Eich T, Fundamenski W, Koslowski H.R, Pitts R.A and JETEFDA Contributors et al 2009 Journal of Nuclear Materials **390-391** 768
[10]. Suttrop W et al 2011 Physical Review Letters **106** 225004
[11]. Huysmans G.T.A and Czarny O, 2007 Nuclear Fusion **47** 659
[12]. Huysmans G.T.A, Pamela S, van der Plas E and Ramet P 2009 Plasma Physics and Controlled Fusion **51** 124012
[13]. Staebler G.M. and Hinton F.L. 1989 Nuclear Fusion **29** 1820
[14]. Kallenbach A, Carlson A, Pautasso G, Peeters A, Seidel U, Zehrfeld H-P and ASDEX Upgrade Team 2001 Journal of Nuclear Materials **290-293** 639
[15]. Harbour P J et al 1989 Journal of Nuclear Materials **162-164** 236
[16]. Takahashi H, Fredrickson E.D. and Schaffer M.J. 2008 Physical Review Letters **100** 205001
[17]. Zheng L.J, Takahashi H and Fredrickson E.D. 2008 Physical Review Letters **100** 115001
[18]. Wingen A, Evans T.E and Spatschek K.H, 2009 Nuclear Fusion **49** 055027
[19]. Wingen A, Evans T.E, Lasnier C.J, and Spatschek K.H. 2010 Physical Review Letters **104** 175001
[20]. Eich T, Herrmann A, Neuhauser J and ASDEX Upgrade Team 2003 Physical Review Letters **91** 195003
[21]. Koslowski H R, Alper B, Borba D.N, Eich T, Sharapov S.E, Perez C.P, Westerhof E and JETEFDA contributors 2005 Nuclear Fusion **45** 201
[22]. Hanson J.D. and Hirshman S.P. 2002 Physics of Plasmas **9** 4410
[23]. Wingen A, Evans T.E. and Spatschek K.H. 2009 Physics of Plasmas **16** 042504
[24]. Evans T.E, Yu J.H, Jakubowski M.W , Schmitz O, Watkins J.G and Moyer R.A 2009 Journal of Nuclear Materials **390-391** 789
[25]. Punjabi A and Verma A 1992 Physical Review Letters **69** 3322
[26]. Nguyen F, Ghendrih P and Grosman A 1997 Nuclear Fusion **37** 743
[27]. Feng Y, Sardei F, Kisslinger J, Grigull P, McCormick K and Reiter D 2004 Contributions to Plasma Physics **44** 57
[28]. Harting D, Wiesen S, Frerichs H, Reiter D, Borner P, Feng Y and JET-EFDA contributors 2011 Journal of Nuclear Materials **415** 540

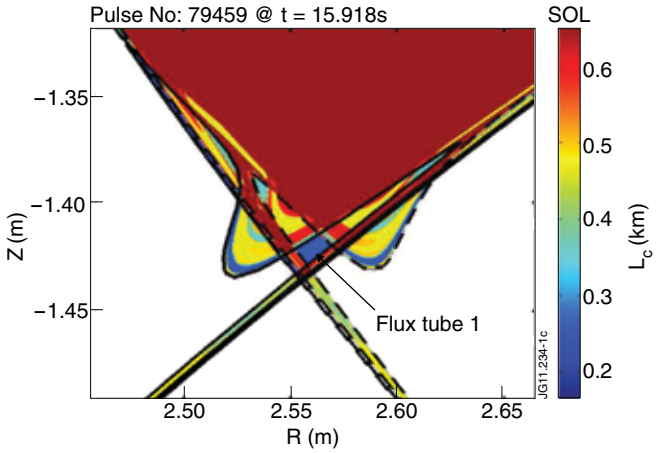

Figure 1: Connection length plot of the poloidal cross-section at φ= 0° of JET discharge JET Pulse No: 79459 at 15.918 s with modelled error fields (I_{EFCC} = 1.6kAt, n = 1). The X-point region is shown. By the intersection of the stable and unstable separatrix manifolds (broken and solid lines, respectively) a short connection length flux tube is created.

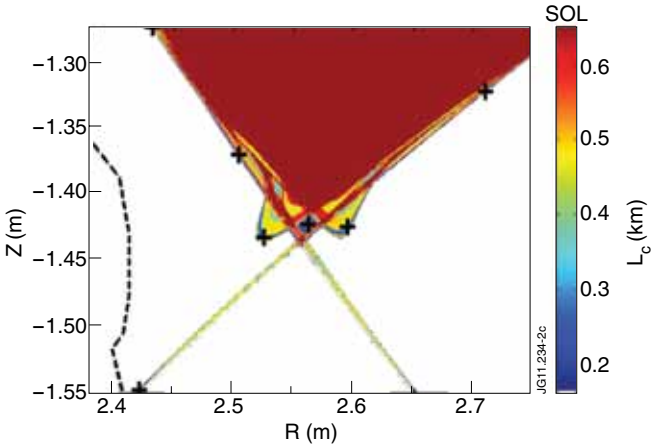

Figure 2: Same as in figure 1. The points of penetration of one field line passing through flux tube 1 are given by the crosses. All observable short connection length regions belong to flux tube 1.

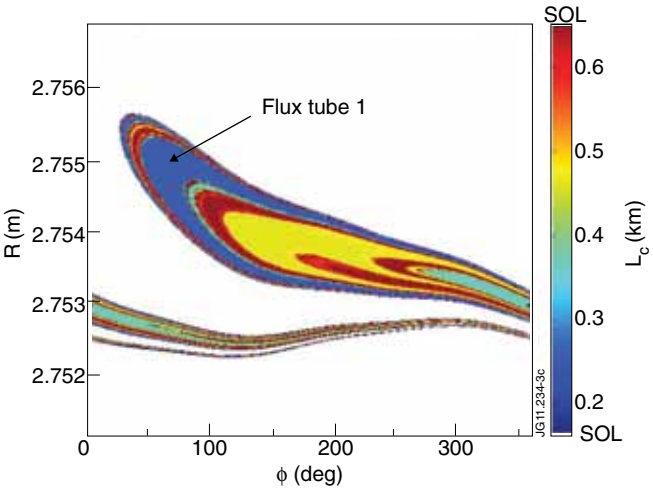

Figure 3: Calculated footprint on the outer target for the same parameters as in figure 1. The area of flux tube 1 has a size of 38.9 cm^2.

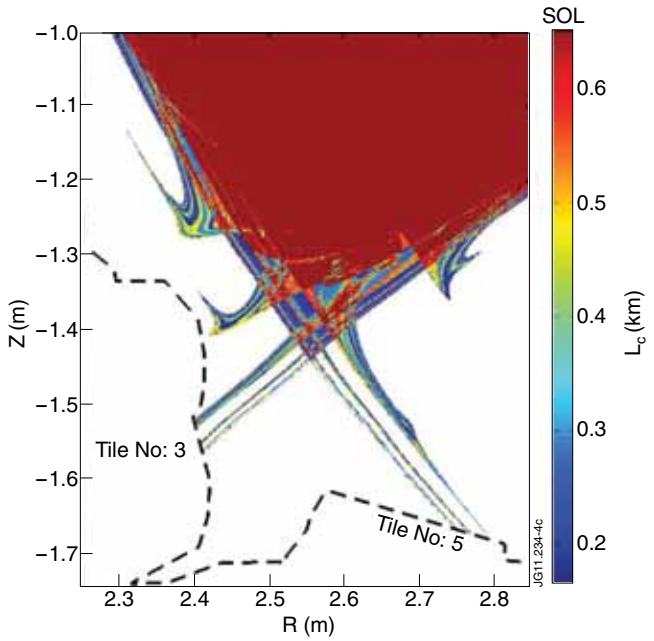

Figure 4: Same as figure 1 with the additional current of 233A in flux tube 1.

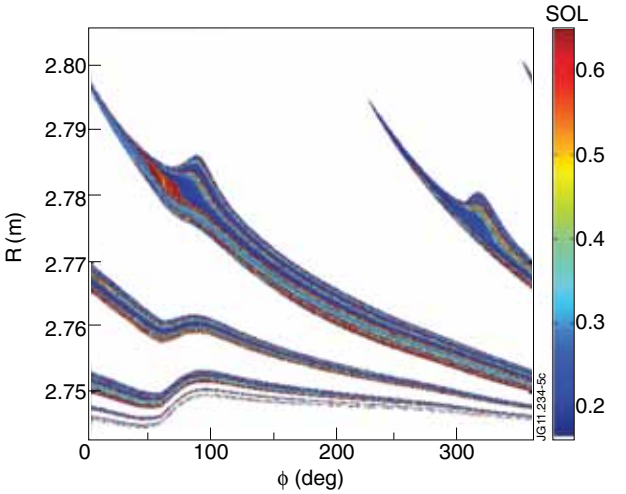

Figure 5: Calculated footprint on the outer target is shown for the same parameter as in figure 4. In comparison to the footprint in figure 3 the footprint has grown considerably in size.

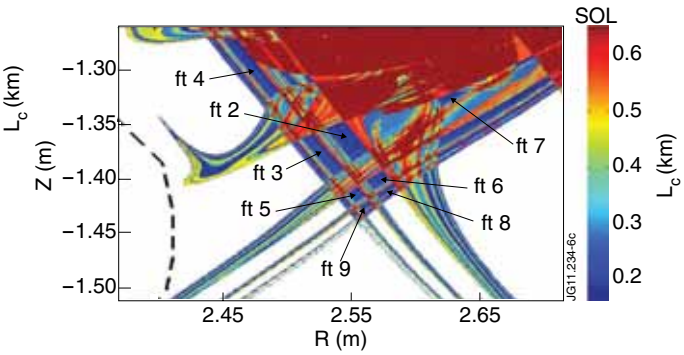

Figure 6: X-point region of the same calculated poloidal cross-section as in figure 4. The large flux tubes are numbered. Unlabelled regions belong to already marked flux tubes.

Flux tube no.	Current (A)
1	233
2	1050
3	798
4	1110
5	218
6	308
7	248
8	151
9	103

JG11.234-10c

Figure 7: Assumed current, carried by the flux tubes. In total an additional current of about 4.2kA is added to the calculation based on the vacuum model.

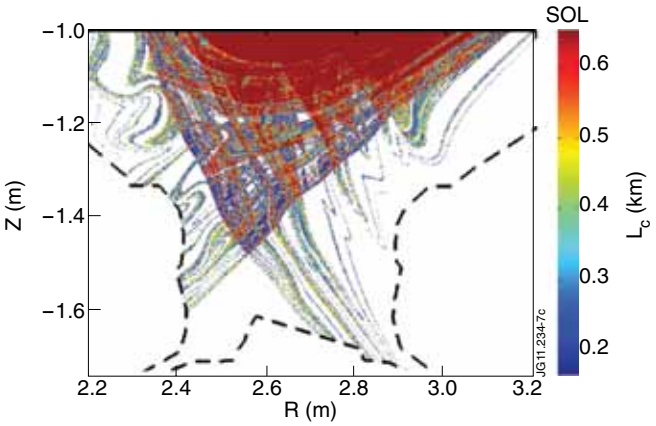

Figure 8: Calculated poloidal cross-section at the toroidal angle that is observed by the infra-red camera for the same parameters as in figure 4 with additional current in flux tubes two to nine. Each flux tube is implemented with one current filament carrying the full current as listed in the table in figure 7.

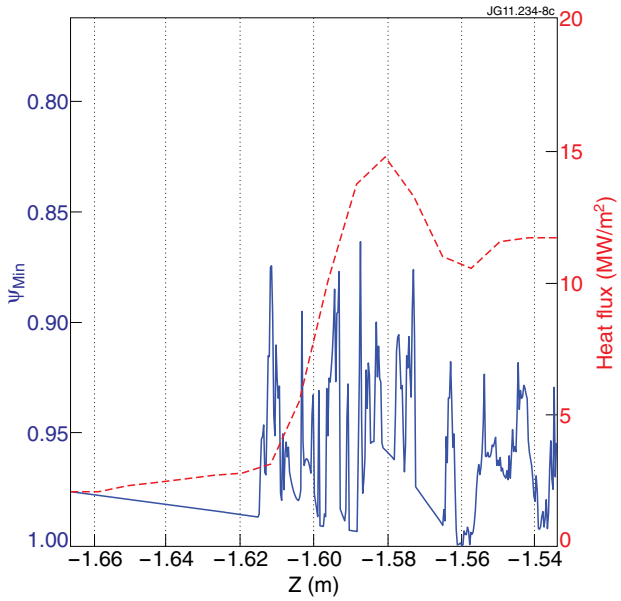

Figure 9: Measured heat flux profile (dashed) compared to the calculated penetration depth profile (solid) at the same position on the inner target (tile #3).

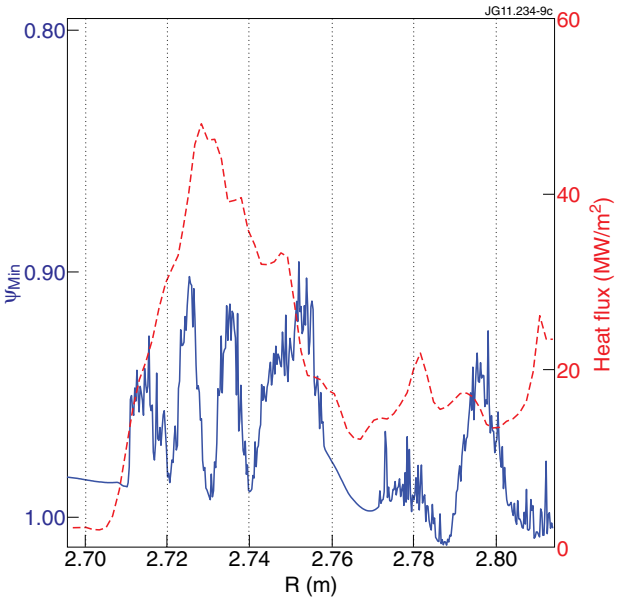

Figure 10: Same as figure 9 for the outer target (tile #5).